
Highlights

- We study the dynamics of quasiperiodically forced circle maps.
- We identify strange nonchaotic attractors as invariant sets that are “weakly chaotic” using the weighted Birkhoff average of rotation vector and Lyapunov exponent as computational tools.
- Efficient numerics distinguishes between strongly chaotic, weakly chaotic, incommensurate, and resonant orbits.

Email addresses: jdm@colorado.edu (J.D. Meiss), esander@gmu.edu (E. Sander)

Resonance and Weak Chaos in Quasiperiodically-Forced Circle Maps

J.D. Meiss^{a,1}, E. Sander^{b,2}

^a*Department of Applied Mathematics, University of Colorado, Boulder, CO, 80309-0526, USA*

^b*Department of Mathematical Sciences, George Mason University, Fairfax, VA, 22030, USA*

Abstract

In this paper, we focus on a numerical technique, the weighted Birkhoff average (WBA) to distinguish between four categories of dynamics for quasiperiodically-forced circle maps. Regular dynamics can be classified by rotation vectors, and these can be rapidly computed to machine precision using the WBA. Regular orbits can be resonant or incommensurate and we distinguish between these by computing their “resonance order.” When the dynamics is chaotic the WBA converges slowly. Such orbits can be *strongly* chaotic, when they have a positive Lyapunov exponent or *weakly* chaotic, when the maximal Lyapunov exponent is zero. The latter correspond to the strange nonchaotic attractors (SNA) that have been observed in quasiperiodically-forced circle maps beginning with the models introduced by Ding, Grebogi, and Ott. The WBA provides a new technique to find SNAs, and allows us to accurately compute the proportions of each of the four orbit types as a function of map parameters.

Keywords: Circle maps, Quasiperiodic forcing, Arnold tongues, Resonance, Birkhoff averages, Strange Nonchaotic Attractors

2020 MSC: 37C55 37E10, 37E45, 65P99, 70K43

Contents

1	Introduction	2
2	Torus Maps: Background	2
3	Regular and Chaotic Orbits	3
3.1	Regular Orbits	4
3.2	Chaos	7
4	Weak Chaos	8
5	Orbit-Type Statistics	10
6	Conclusions	12
Appendix A	Weighted Birkhoff Averages	13
Appendix B	Resonance Orders	14

Email addresses: jdm@colorado.edu (J.D. Meiss), esander@gmu.edu (E. Sander)

¹JDM was supported in part by the Simons Foundation under Award 601972. Useful conversations with Nathan Duignan are gratefully acknowledged.

²ES was supported in part by the Simons Foundation under Award 636383.

1. Introduction

It has been conjectured that for typical dynamical systems three types of maximal invariant sets are observable: periodic, topological tori with quasiperiodic dynamics, and chaotic [39]. Here we use weighted Birkhoff averages (WBA) [6, 8, 37], to study this question for quasiperiodically forced circle maps. The WBA allows for quick and accurate distinction between regular and chaotic orbits and also provides a highly accurate calculation of rotation vectors for regular orbits—it is super-polynomially convergent for Diophantine vectors [10]. Given an accurate computation of a frequency, the method of resonance orders [32] distinguishes between those that are numerically incommensurate and commensurate. Combining these techniques, we are able to quickly classify orbits as chaotic, resonant, or quasiperiodic on a torus in one or more dimensions.

Alternative algorithms for computing rotation vectors and sets include [1] for circle maps, the set-based methods in [34] for torus maps, and methods for numerical continuation of invariant tori [36]. The parameterization method can be used to explicitly compute the conjugacy to rigid rotation [20], and the needed rotation vector can be efficiently computed using the WBA [4]. The frequency analysis method of Laskar [26, 27] uses a Hanning window to give a quadratically convergent Fourier amplitudes to compute rotation vectors. In a series of papers Villanueva and collaborators use Richardson extrapolation to estimate rotation numbers for analytic circle diffeomorphisms [40, 28, 41, 29, 44]. Experimentally, this appears to give super-convergence for Diophantine irrationals, but the convergence has not been rigorously shown. For a comparison of many of these methods to the WBA, see the discussion in [8].

In this paper, we use the WBA to distinguish between regular and chaotic orbits for quasiperiodically forced circle maps. Though these are two-dimensional they still retain some of the behavior of one-dimensional maps; for example, when the map is a homeomorphism then every orbit has the same rotation vector [21]. These maps can have strange nonchaotic attractors (SNA), i.e., geometrically “strange” attractors that have nonpositive Lyapunov exponents [11, 43, 33, 18]. In the classic examples [21, 19], SNAs are weakly chaotic—exhibiting sensitive dependence on initial conditions but not exponential divergence [17]. It was previously shown that the WBA identifies SNAs for the forced-damped pendulum [12]. We show here that the WBA identifies strange nonchaotic attractors in forced circle maps.

The main focus of the paper is to use the WBA to distinguish between regular (either incommensurate or resonant) and chaotic behavior. In §2 we briefly recall some of the theoretical background for torus maps. The appendices recall the numerical methods we developed in [37, 32]: [Appendix A](#) explains how to use the WBA to compute rotation vectors and how it gives an efficient method to identify chaos. In [Appendix B](#) we recall the method of “resonance orders” to distinguish resonant (lower-dimensional) invariant tori from those that are nonresonant (full-dimensional). We apply these techniques in §3 to classify the orbits of two-dimensional torus maps with a rigidly rotating second component. In §4 we show how the WBA together with Lyapunov exponents can be used to distinguish strongly chaotic orbits from those that are weakly chaotic. In §5 we compute the proportions of the four categories of orbits—resonant, incommensurate, weakly chaotic and strongly chaotic—as a function of the parameters of the map. We conclude in §6.

2. Torus Maps: Background

We begin by recalling some of theoretical background for torus maps $f : \mathbb{T}^d \rightarrow \mathbb{T}^d$ that are homotopic to the identity. If $\pi : \mathbb{R}^d \rightarrow \mathbb{T}^d$ is the standard projection, then a map $F : \mathbb{R}^d \rightarrow \mathbb{R}^d$ is a lift of f if

$$\pi \circ F = f \circ \pi.$$

Here we take the period of the torus to be one, so that $F(x) \bmod 1 = f(x \bmod 1)$. Since f is homotopic to the identity, $F(x+m) = F(x) + m$ for each $m \in \mathbb{Z}^d$, i.e., the map has degree one. Note that any two lifts, say F_1 and F_2 , differ by an integer vector $F_1(x) = F_2(x) + m$ —indeed this must be true for any fixed x , but by continuity the same vector m must work for all x .

In general we can assume that a degree-one torus map has the form

$$x' = f(x) = x + \Omega + g(x; a) \mod 1, \quad (1)$$

where $\Omega \in \mathbb{T}^d$, a is a parameter vector, and g is periodic, $g(x + m; a) = g(x; a)$ for any $m \in \mathbb{Z}^d$ (and every a). This simplest case is Arnold's circle map, where $d = 1$, and

$$g(x; a) = \frac{a}{2\pi} \sin(2\pi x).$$

In §3 we consider quasiperiodically-forced circle maps, where $d = 2$ and (1) is of the form

$$f(x_1, x_2) = (f_1(x_1, x_2), x_2 + \Omega_2),$$

with $\Omega_2 \in \mathbb{R} \setminus \mathbb{Q}$, i.e., it is a skew product and the second component is a rigid rotation with irrational rotation number. A commonly studied example extends the Arnold map, using the form (1) with

$$g(x_1, x_2) = \frac{1}{2\pi} \begin{pmatrix} a_1 \sin(2\pi x_1) + a_2 \sin(2\pi x_2) \\ 0 \end{pmatrix}. \quad (2)$$

Such maps have been studied in [11, 15, 33, 42, 24, 22, 18].

The orbit of $x \in \mathbb{T}^d$ has (pointwise) rotation vector $\omega \in \mathbb{T}^d$ if the limit

$$\omega(x, f) = \lim_{t \rightarrow \infty} \frac{F^t(x) - x}{t} \mod 1 \quad (3)$$

exists. This is independent of the choice of lift; however, it can depend upon the initial point.

The quasiperiodically-forced map (1) with (2) is a homeomorphism whenever $|a_1| \leq 1$. Herman showed that whenever a skew product map on \mathbb{T}^2 is a homeomorphism, then every orbit has a rotation number that depends continuously on f and moreover that the limit (3) is independent of x [21, 42]. When the map is a homeomorphism, the graph $\{\omega_1(x, f) : \Omega_1 \in \mathbb{R}\}$ for fixed a_1, a_2 , and Ω_2 , is monotone increasing [3].

Note that since the quasiperiodic map has a trivial second component,

$$\omega_2(x, f) = \Omega_2. \quad (4)$$

Moreover, when $a_1 = 0$,

$$\omega_1 = \lim_{t \rightarrow \infty} \frac{1}{t} \left(t\Omega_1 + \frac{a_2}{2\pi} \sum_{j=0}^{t-1} \sin(2\pi(j\Omega_2 + x_2(0))) \right) = \Omega_1, \quad (5)$$

since the trigonometric terms average to zero. Thus for $a_1 = 0$, $\omega(x, f) = \Omega$ for any a_2 and any x .

More generally, the convergence of the limit (3), if it exists, can be slow, especially when the orbit is chaotic or the system has a strange nonchaotic attractor [11, 15, 42]. Instead of (3), we compute the weighted Birkhoff average

$$\omega_T = WB_T(F(x) - x) = \Omega + WB_T(g(x; a)), \quad (6)$$

using T iterates, see (A.2). As noted in Appendix A, the WBA accelerates the convergence of the pointwise rotation vector (3) especially when the orbits are not chaotic.

3. Regular and Chaotic Orbits

In this section we study the map (1) with the force (2). In this paper we think of Ω_2 primarily as a “structural parameter,” fixing it to be

$$\Omega_2 = \gamma \equiv \frac{1}{2}(\sqrt{5} - 1) \approx 0.618034, \quad (7)$$

the inverse of the golden mean. It is computationally infeasible to perform a detailed parameter study to determine how the dynamical behavior depends on the three remaining parameters (Ω_1, a_1, a_2) . In most cases, we will study the dependence upon (Ω_1, a_1) for fixed a_2 , but in several cases we will instead fix a_1 and vary (Ω_1, a_2) .

3.1. Regular Orbits

Since the x_2 dynamics for (2) is a rigid rotation and $\omega_2 = \Omega_2 = \gamma$ is irrational, each orbit $\{(x_1(t), x_2(t)) : t \in \mathbb{N}\}$ is dense on $x_2 \in [0, 1]$. One way to visualize these dynamics is to take a Poincaré section, say at $x_2 = 0$; however, since the orbit is discrete we instead use a “Poincaré slice,” plotting points at a sequence of times t_j for which $|x_2(t_j)| < 0.0005$, see Fig. 1. In this figure we use the criterion (A.6) to select only the *nonchaotic* orbits, those for which the WBA has converged to at least nine digit accuracy, $\text{dig}_T \geq 9$, after $T = 10^6$ iterates. The vertical axis in the figure is the image

$$x_1(t_j + 1) = f_1(x_1(t_j), x_2(t_j)) \approx f_1(x_1(t_j), 0),$$

which is the Arnold function. Thus when a_2 is sufficiently small the resulting figure can be viewed as a perturbation of the one-dimensional Arnold map. Indeed, even when $a_2 = 0.6$, in panel (a), the resulting orbits resemble those that one would see in Arnold’s map, and there are many regions with incommensurate frequency vectors (small dots), separated by resonant tongues, regions where $m \cdot \omega = n$ for some nonzero $(m, n) \in \mathbb{Z}^3$ (large dots) see (B.1). Note that a resonant tongue corresponds to the existence of an attracting invariant circle on \mathbb{T}^2 . When m_1 and $m_2 \neq 0$ these resonances have irrational ω_1 :

$$\omega_1 = \frac{n}{m_1} - \frac{m_2}{m_1} \gamma \in \mathbb{R} \setminus \mathbb{Q}. \quad (8)$$

Computing the resonance order and using criterion (B.6) for Fig. 1(a), where $a_1 = 0.8$, we find ω is incommensurate for 26.7% of the orbits, while it is resonant for 72.3% (the remaining 1% are chaotic and not shown here). By contrast, in panel Fig. 1(b) where $a_2 = 2.49$, only 2% are incommensurate while 94.7% of the orbits are resonant (3.3% are chaotic). Finally for $a_2 = 5$ in panel (c), 1.1% are incommensurate, while 96.8% are resonant (2.1% are chaotic).

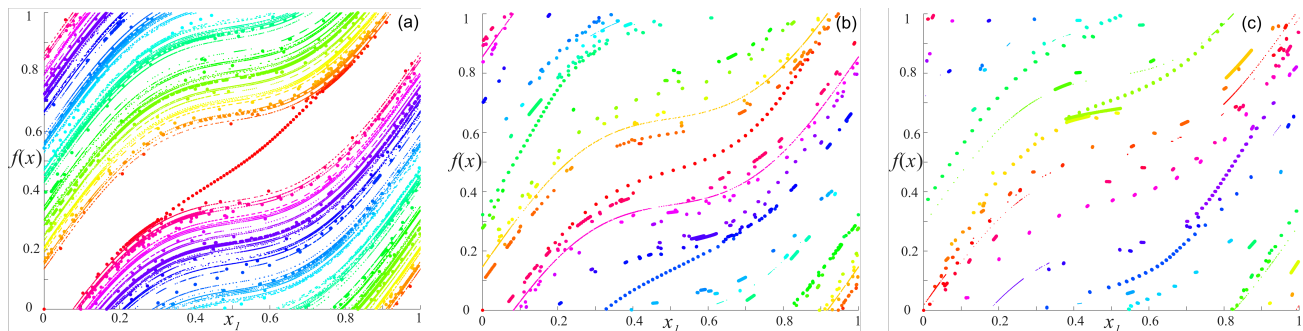


Figure 1: Poincaré slices of regular orbits of the quasiperiodically-forced circle map with $a_1 = 0.8$ and $\Omega_2 = \gamma$, for (a) $a_2 = 0.6$, (b) $a_2 = 2.49$ and (c) $a_2 = 5$ (these are the first, fourth, and eighth values shown in Fig. 8). The plot shows a grid of 200 for $\Omega_1 \in [0, 1]$, with the orbits colored as in Fig. 2 using the value of ω_1 computed with $T = 10^6$. Resonant orbits are plotted with larger dots. Each orbit is iterated 10^5 times to remove transients, and the next 1000 points on the Poincaré slice $|x_2| < 0.0005$ are shown.

The rotation number ω_1 for nonresonant and resonant orbits is shown as a function of (Ω_1, a_1) in Fig. 2 for $a_2 = 0.6$ (top panels) and $a_2 = 1.0$ (bottom panels). These use a grid of 1000×1000 evenly spaced values of $(\Omega_1, a_1) \in [0, 1] \times [0, 2]$, with Ω_1 slightly shifted away from rationals to avoid resonances at $a_1 = 0$. Each orbit begins at the same randomly selected point $(x_1(0), x_2(0))$ and is initially iterated 10^4 times to remove transients. To compute both ω_T and dig_T we use $T = 10^6$. As noted by [11], the nonresonant regions (left panels) as a function of (Ω_1, a_1) , look similar to the circle map case when a_2 is small; however, note that the proportion of the nonresonant orbits appears to fall essentially to zero for a value of a_1 smaller than 1, unlike the Arnold case (see §5, below).

The parameters with resonant orbits are shown in Fig. 2(b) and (d) for the same values of a_2 . These are analogous to the tongues or mode-locking regions of the Arnold map; for example, the $\omega_1 = \frac{0}{1}$ (red), $\frac{1}{1}$

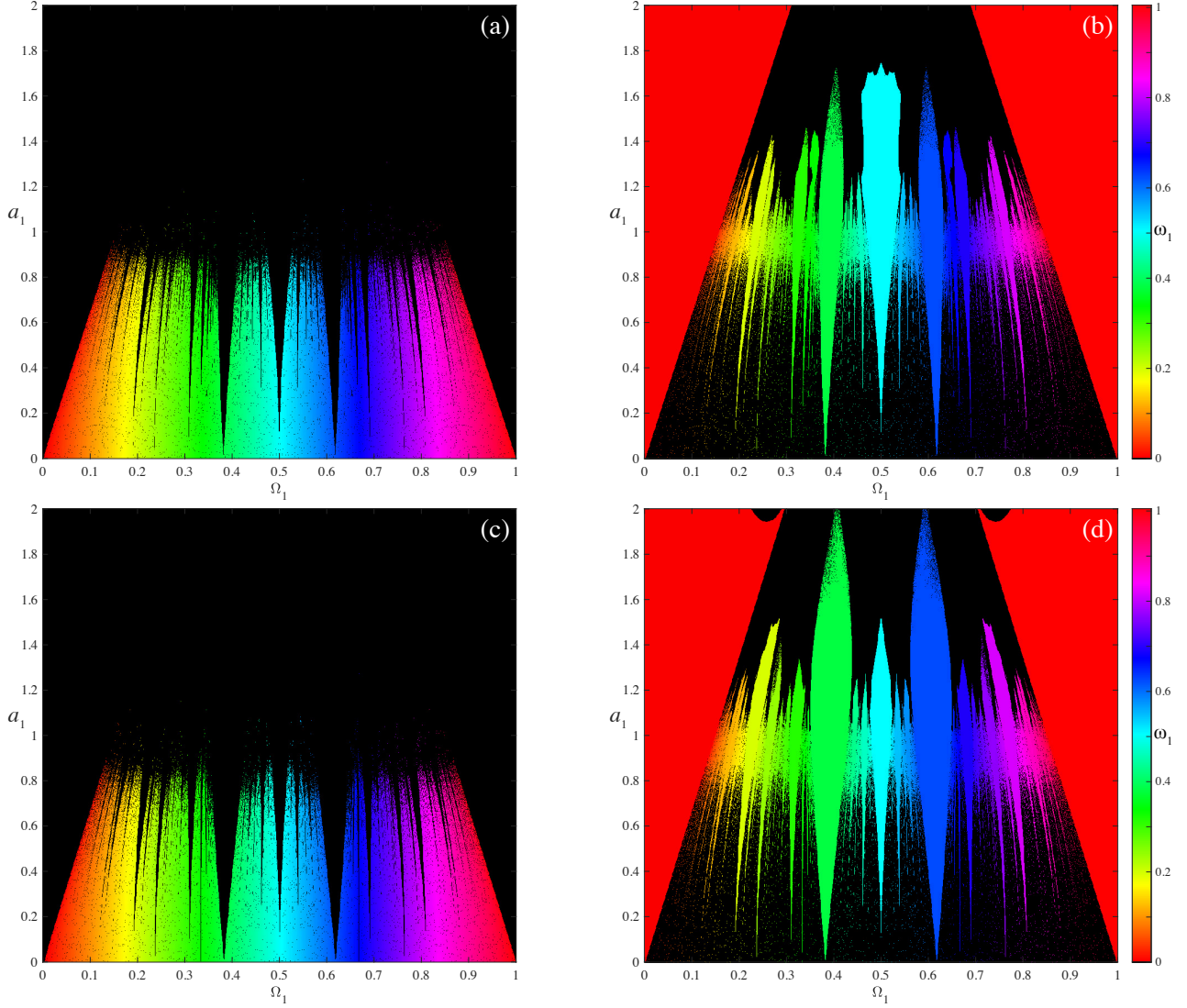


Figure 2: Nonresonant (panels (a) and (c)) and resonant (panels (b) and (d)) orbits for the quasiperiodically-forced circle map (2) as a function of (a_1, Ω_1) for $a_2 = 0.6$ (top panels) and $a_2 = 1$ (bottom panels), with $\Omega_2 = \gamma$ (7). These orbits are distinguished using (A.6) and (B.6). The orbits are colored using ω_1 as shown in the color bars with black indicating no orbits of the given type.

(red) and $\frac{1}{2}$ (cyan) tongues are prominent. However, rank-one resonances with $m_2 \neq 0$ (8) create additional tongues. Perhaps the most prominent new mode-locking regions are those with $(m, n) = (1, 1, 1)$, so that $\omega_1 = 1 - \gamma \approx 0.382$ (green) and with $(m, n) = (1, -1, 0)$ so that $\omega_1 = \gamma \approx 0.618$ (blue). Like the Arnold tongues, these have cusps when $a_1 = 0$ at $\Omega_1 = \omega_1$ and broaden as a_1 increases. Note however that unlike the Arnold map, the resonant regions do not monotonically increase in width when a_1 exceeds 1. These “leaf shaped” tongues were observed in [14].

An alternative view of the tongues is seen in Fig. 3, which shows the resonant regions for fixed $a_1 = 1.2$ on a 2000×2000 grid of $(\Omega_1, a_2) \in [0, 1] \times [0, 20]$. The larger tongues in the figure are labeled by the computed resonance vector (m_1, m_2, n) . Note that we can accurately compute these regions since, by (A.6), we find ω_1 with precision at least 10^{-9} . Feudel et al [14] observed that for a_1 fixed, the widths of the tongues oscillate

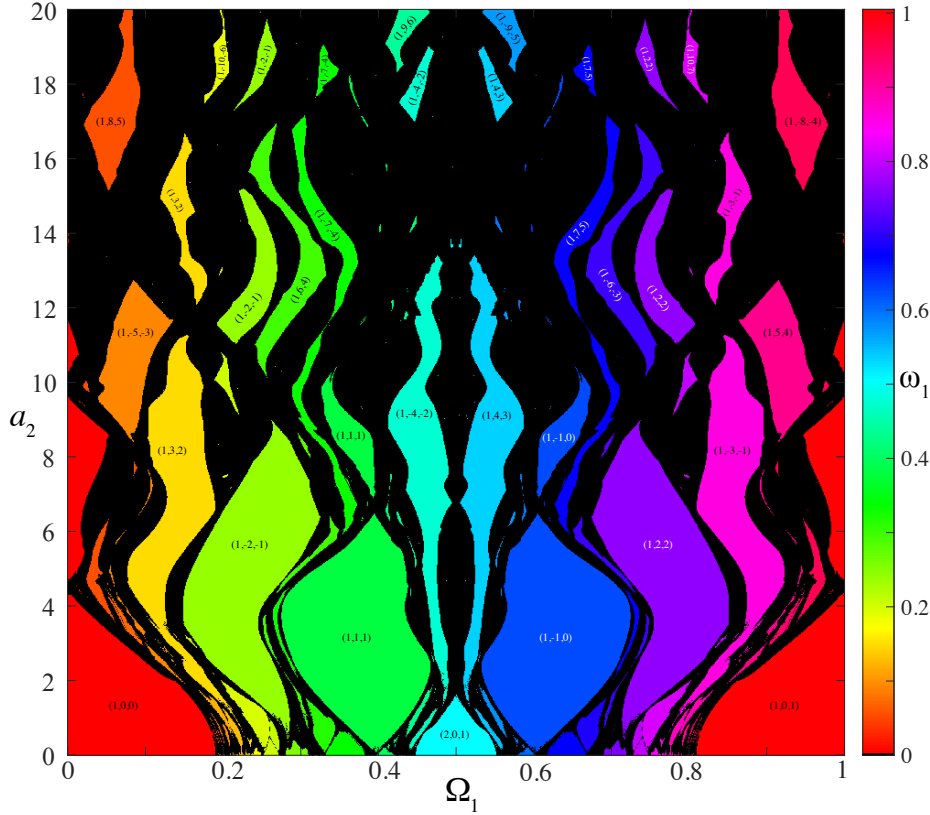


Figure 3: Resonant regions for the quasiperiodically-forced circle map (2) for $a_1 = 1.2$. The larger regions are labeled by (m_1, m_2, n) , Each resonance is colored by ω_1 and black regions correspond to either chaotic or incommensurate orbits.

and narrow over intervals as a_2 increases; this is referred to as *pinching*. In Fig. 3, some of the resonance tongues appear to pinch off completely, forming a sequence of “bubbles” or “isolas”. However, in general pinching does not require the width to become zero. As noted in [33], there can be multiple attracting orbits within a tongue (and these can give rise to SNAs, see §4).

In a previous study of resonant tongues, [33] computed the tongues using bifurcation curves, concentrating on the case $\omega_1 = 0$, i.e., $(m, n) = (1, 0, 0)$. For example, in [33, Fig. 2] Osinga et al observe that when $a_1 = 0.8$ the first pinching occurs for $4.1 < a_2 < 4.8$; this corresponds to a region of bistability for several invariant circles. They note that the formation of the pinches is associated with bifurcations in which a pair of invariant circles collide at a dense set of points but the collision is not smooth (this is also related to SNAs, see §4). In addition, [14] study the case $a_1 = 1$ with $a_2 \in [0, 2\pi]$. Figure 5 of [33] shows the $(m, n) = (1, 0, 0)$ tongue first pinches at $a_2 = 4.7$, the $(2, 0, 1)$ tongue at $a_2 = 3.0$, and $(3, 0, 1)$ at $a_2 = 0.9$. Glendinning et al [16] show that the width of the $(1, 0, 0)$ resonance region is asymptotically $|J_0(a_2/(2\sin(\pi\gamma)))|$, for $a_2 \gg 1$ and $a_1 \ll 1$. Here J_0 is the Bessel function; thus its zeros determine the pinching points in a_2 , and the width approaches zero as $\mathcal{O}(a_2^{-1/2})$ for large coupling. This formula predicts the first pinch at $a_2 = 4.48$. A similar result for $(m, n) = (1, -k, 0)$, involves the Bessel function J_k instead of J_0 , reflecting the zero width of these tongues at $a_2 = 0$. The actual bifurcation do not always pinch; they can have two or more folds bounding small regions of multi-stability—[33] shows that these correspond to saddle-node/pitchfork bifurcations of multiple circles.

Our computations are consistent with these previous results. For example, for $a_1 = 0.8$ (not shown), we observe that the $(1, 0, 0)$ tongue first pinches at $a_2 = 4.51$, though it does not pinch off completely; for

$a_1 = 1.2$, the red region in Fig. 3, the first pinch point occurs at $a_2 = 4.40$ and the second at 9.63. For the $(2, 0, 1)$ tongue we observe pinch points at $(a_1, a_2) = (0.8, 2.04)$, $(0.8, 3.96)$, and $(1.2, 1.64)$. The $(3, 0, 1)$ tongue is significantly thinner for both a_1 values and is not labelled in Fig. 3; when $a_1 = 1.2$, its first pinch point occurs at $a_2 = 0.66$.

Note that most of the tongues considered in previous works correspond to the special case of $(m_1, 0, 1)$ resonances. However, as we see in Fig. 3, these are not the most prominent cases: they are only present for small a_2 and appear to disappear entirely as a_2 grows. We also observe that $m_2 \neq 0$ resonances are most prominent when $a_1 = 0.8$ (not shown).

3.2. Chaos

Orbits that are identified as chaotic by (A.6) are shown in Figs. 4-5. Instead of using ω_1 for the color scheme—as we did in the previous figures—the colors indicate the Lyapunov exponent. For the nonlinearity (2) this is particularly easy to compute since the Jacobian of (1) is upper triangular:

$$Df = \begin{pmatrix} 1 + a_1 \cos(2\pi x_1) & a_2 \cos(2\pi x_2) \\ 0 & 1 \end{pmatrix}.$$

This implies that one of the Lyapunov exponents is zero and the other is simply the time average

$$\lambda = \lim_{t \rightarrow \infty} \frac{1}{t} \sum_{j=0}^{t-1} \ln |1 + a_1 \cos(2\pi x_1(j))|, \quad (9)$$

if this limit exists. Since (9) is the time average of a scalar function on phase space, we can also easily compute it using (A.2):

$$\lambda_T = WB_T(\ln |1 + a_1 \cos(2\pi x_1)|). \quad (10)$$

The average (10) was previously used in [8] to show that both Lyapunov exponents are zero for nonchaotic, nonresonant orbits of a torus map.

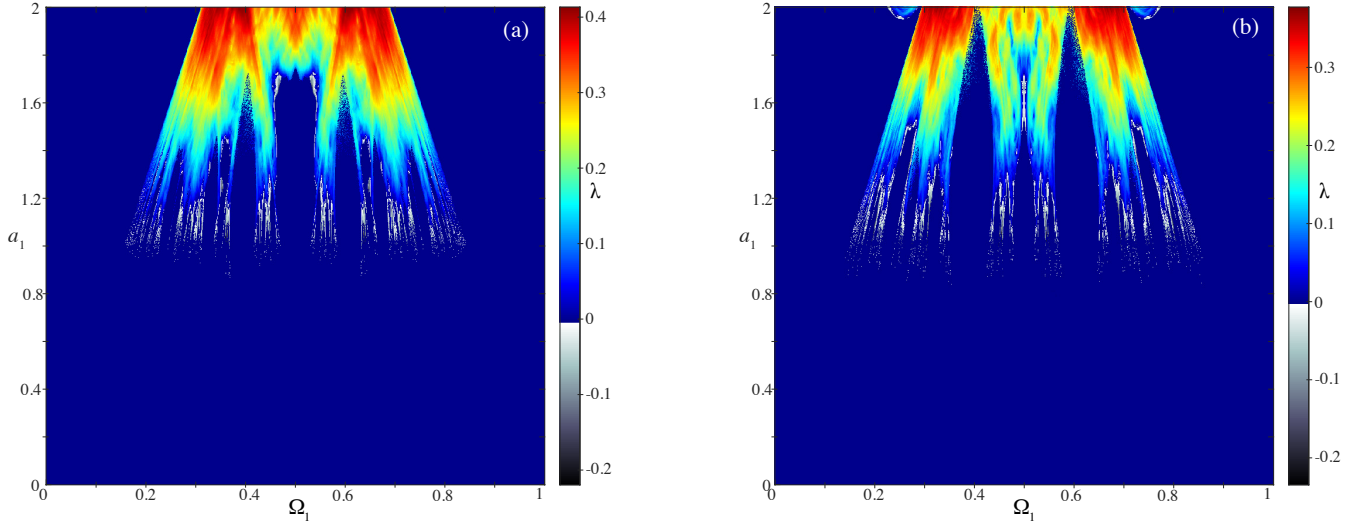


Figure 4: Chaotic orbits of the quasiperiodically-forced circle map (2) for a 1000×1000 grid in the (Ω_1, a_1) plane for (a) $a_2 = 0.6$ and (b) $a_2 = 1$. The color bar corresponds to λ_T (10). Parameters with $\lambda_T \leq 0$ are gray; they correspond to weak chaos, or strange nonchaotic attractors. Parameters with nonchaotic orbits are colored dark blue, and strongly chaotic orbits have colors that vary with λ_T .

Of course, a weighted average like (10) should not be expected to improve convergence for orbits that are chaotic; however, when the orbit is periodic or quasiperiodic, we expect that λ_T should converge more rapidly than (9). Indeed our tests show that this is the case when $\lambda \leq 0$. For example, using a 500×500 portion of the grid in (Ω_1, a_1) , we find that when $a_2 = 0.6$ approximately 70% have $\lambda_T \leq 0$ for $T = 10^6$. For these regular cases, if we instead use a much smaller number of iterates, $T = 800$, we found the mean error $\langle \text{dig}_T \rangle = 3.6$ for (9), while $\langle \text{dig}_T \rangle = 7.9$ for (10). This more rapid convergence of (10) persists as T is increased.

Note that if $|a_1| > 1$ the function being averaged in (10) is not smooth, and since the weighted average relies on smoothness for improving convergence, we would not expect (10) to be helpful. Moreover, the only case for which the weighted average has been proven to be super-convergent is for orbits conjugate to a rigid quasiperiodic rotation [10]: there are no such orbits when $|a_1| > 1$. Nevertheless the less accurate computations of the Lyapunov exponent still do indicate that $\lambda_T > 0$ for many orbits as a_1 grows in Fig. 4. There are also orbits in these panels that are chaotic according to (A.5), but for which $\lambda_T \leq 0$ —they are shown in gray in Figs. 4-5; we discuss these next.

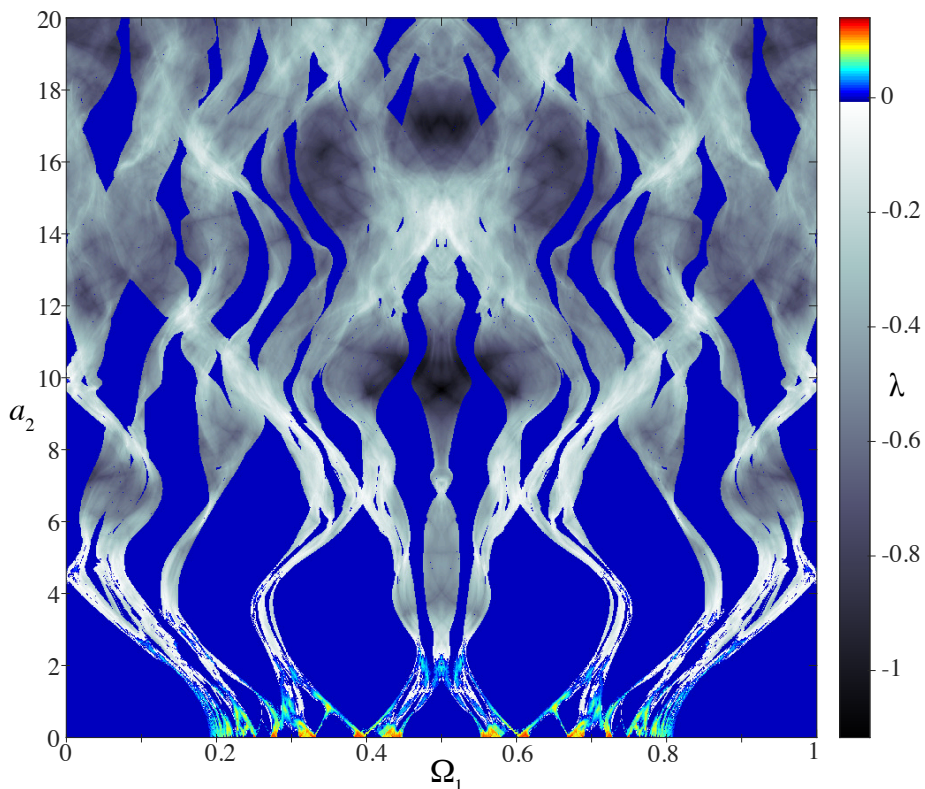


Figure 5: Quasiperiodically-forced circle map (2) for $a_1 = 1.2$ for a 1000×1000 grid in (Ω_1, a_2) showing orbits with sensitive dependence using Criterion (A.5), colored by Lyapunov exponent (10). The grayscale indicates strange nonchaotic attractors. Blue indicates nonchaotic parameters, most of which correspond to the resonance regions in Fig. 3.

4. Weak Chaos

It was first observed by [11] that there is a range around $a_1 = 1$ for which quasiperiodically-forced circle maps can exhibit strange nonchaotic attractors (SNAs), defined to be attractors that are geometrically strange, but which have $\lambda \leq 0$. In some cases [17] showed that SNAs correspond to “weak chaos,” meaning

sensitive dependence on initial conditions; we will use the terms weak chaos and SNA interchangeably. In particular, the criterion (A.5) combined with negative Lyapunov exponent serves as a new criterion for weak chaos/SNA:

$$\text{dig}_T < D_T \text{ and } \lambda_T \leq 0 \Rightarrow \text{“weakly chaotic”} . \quad (11)$$

Alternatively when $\lambda > 0$ we refer to the orbit as having “strong chaos”, or—more simply—as chaotic. An example is shown in Fig. 6(a); this is an orbit of (1) and (2) with $\text{dig}_T = 8.4 < D_T$ and $\lambda_T = -0.0648 < 0$, so it satisfies (11). Visually, the phase portrait shows the expected geometric “strangeness”. Since we use the convergence rate of the WBA to detect chaos and not the geometry of the orbit, our criterion (11) differs significantly from previously used methods to identify SNA.

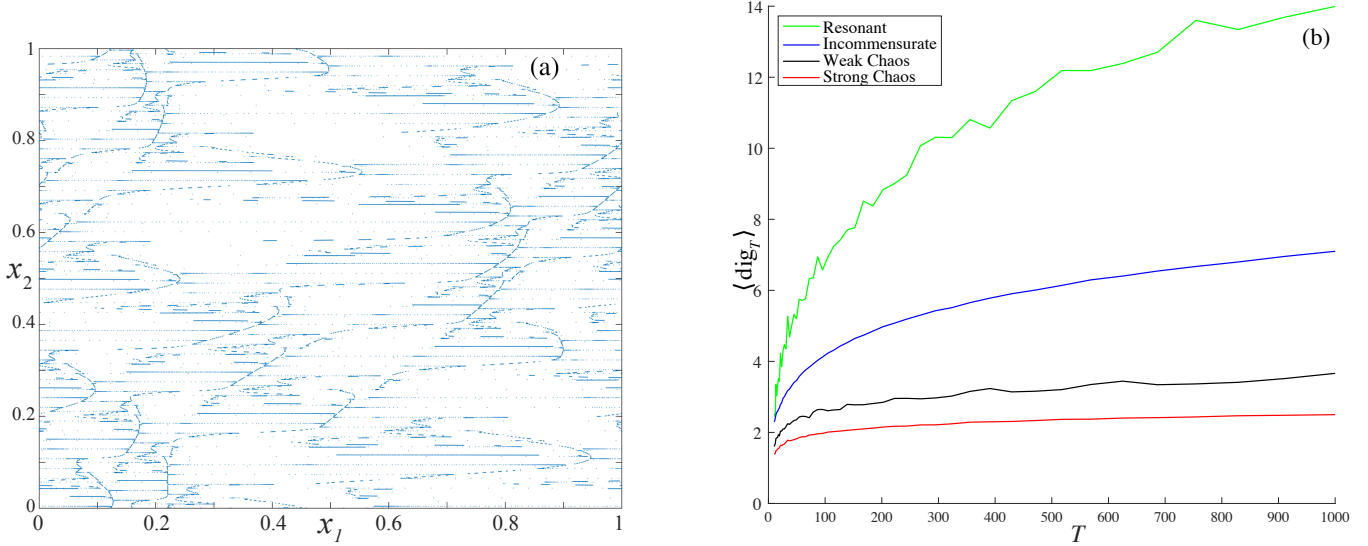


Figure 6: (a) A phase portrait of a weakly chaotic orbit for (2) with $(a_1, a_2) = (0.93493, 1)$ and $\Omega_1 = 0.5526$. (b) The mean value of dig_T as a function of $T \in [0, 1000]$ for (2) with $a_1 \in [0, 2]$, $a_2 = 1$ and $\Omega_1 \in [0, 1]$. The orbits are separated into four types: strongly chaotic orbits have the smallest $\langle \text{dig}_T \rangle$ (red), followed by weakly chaotic orbits (black), nonresonant (blue), and finally resonant orbits (green). Out of the 10^6 orbits sampled, 4213 were identified as weakly chaotic. For comparison we randomly selected 4213 orbits of each of the other types.

For the example in Fig. 6(a), $|a_1| < 1$ so the rotation number does exist and is independent of initial condition; however, as was emphasized in [42] the convergence of (3) can be slower than T^{-1} . Stark et al constructed an algorithm that is guaranteed to converge as T^{-1} by averaging over initial conditions. To compute this, they use a discrete approximation to the integral on a grid $x_2(0) = \frac{i}{N}$, $i = 0, \dots, N$, to obtain

$$\omega^{Stark} = \frac{1}{NT} \sum_{i=0}^{N-1} (f^T(x_1, \frac{i}{N}) - (x_1, \frac{i}{N})) . \quad (12)$$

For example, when $(a_1, a_2) = (0.8, 6\pi)$, and $\Omega_1 = 0.01$, the map has an SNA according to [15]. Using $N = 10^3$ and $T = 10^5$, in (12), [42] computed

$$\omega_1^{Stark} = 0.0173598 .$$

When we use (6) to compute ω_T with $T = 10^6$ we obtain the same value to the quoted accuracy, and find $\text{dig}_T = 6.4$, which is consistent with six digits accuracy. For this case, $\lambda_T = -0.2646098$, so by Criterion (11) this orbit is indeed weakly chaotic. This example, and others that we have tried, show that the WBA can give the same accuracy as (12) with a factor of 50 fewer iterates!

We show in Fig. 6(b) that there are distinct differences in the number of digits, dig_T , for the four categories of orbits: resonant, incommensurate, weakly chaotic, and strongly chaotic. Here we selected orbits from the data in Fig. 2 and Fig. 4 with $a_2 = 1$. Of the 10^6 orbits, 4213 were identified as weakly chaotic using (11). The black curve in the figure shows the average $\langle \text{dig}_T \rangle$ for these orbits as a function of T . For a fairer comparison, we randomly selected the same number of orbits of the other three types. Note that for each T in Fig. 6(b), $\langle \text{dig}_T \rangle$ is ordered monotonically by type; it is largest for the resonant orbits, smaller for the incommensurate case, smaller for weak chaos and finally smallest for strong chaos. In particular, ω_T for the resonant orbits nearly reaches double precision accuracy (at least in the mean) even for $T = 1000$. In addition, the rate of increase of dig_T with T is also ordered in the same way by type; however, the distinction in rates between the weakly and strongly chaotic orbits is less pronounced. Nevertheless, even though these distinctions are clear for the average $\langle \text{dig}_T \rangle$, this method does not give a reliable classification: the values of dig_T for individual orbits can vary significantly.

5. Orbit-Type Statistics

The proportions of orbits of each of the four types—strongly chaotic (red), weakly chaotic (black), resonant (green) and incommensurate (blue)—are shown in Fig. 7. This figure uses the data in Fig. 2 and Fig. 4, summed over Ω_1 , as a function of a_1 for two fixed values of a_2 .

Note that the curves for the incommensurate orbits (blue) should begin at 1 when $a_1 = 0$ according to (5); however, our method underestimates this fraction by about 1.5%, declaring that orbits with orders outside the interval (B.6) are resonant. Some cutoff is inevitable, of course, since we cannot compute with infinite precision; moreover, a given precision δ results on average in a smaller resonance order in higher dimensions: compare the factor of $\frac{1}{3}$ in (B.5) with the factor $\frac{1}{2}$ for the 1D case in [37]. The incommensurate fraction in Fig. 7 drops nearly to zero with a shape similar to the power law behavior seen for a circle map [13, 38], but in contrast to the 1D case, it becomes nearly zero when a_1 is below 1.0; this corresponds to the onset of weak chaos (black curves). Of course, when $a_1 > 1$, there are no incommensurate orbits, and our method falsely identifies very few.

The fraction of resonant orbits (green) no longer has the cusp at $a_1 = 1$ that is seen for a circle map [38], and it now decreases more substantially when $a_1 > 1$. This, of course could be anticipated from the right panels of Fig. 2, since the widths of some of the resonant tongues decrease for $a_1 > 1$.

The proportion of weak chaos (black) is largest when a_1 is just above 1: in Fig. 7(a) where $a_2 = 0.6$, this fraction is larger when $a_1 \in (1, 1.2)$ with a peak of about 10%; the same height is seen in panel (b), where $a_2 = 1$, but the range over which there is weak chaos broadens. In both cases there is nonzero fraction of weak chaos over a wider range.

The chaotic fraction in Fig. 7 (red) is nonzero for $a_1 > 1$ and grows to about 40% when $a_1 = 2$, which is larger than that found for a circle map [38].

Figure 8(a) shows the parameters exhibiting strong chaos (red) and weak chaos (black) for eight values of $a_2 \in [0.6, 5]$ (vertical axis) as a function of $(\Omega_1, a_1) \in [0, 1] \times [1, 2]$ (horizontal axes). As was also seen in Fig. 5, the relative proportion of weak chaos continues to grow as a_2 increases. This three-dimensional view of the data fits together the viewpoints in Fig. 2 and Fig. 4, which fix a_2 and plot (Ω_1, a_1) , and Fig. 3 and Fig. 5, which fix a_1 and plot (Ω_1, a_2) .

The proportion of the four orbit types as a function of a_1 is shown in Fig. 8(b) for each of the eight values of a_2 from Fig. 8(a). Here increasing thickness of the curves is used to indicate increasing values of a_2 . As we noted in Fig. 7, the proportion of incommensurate orbits (blue curves) are underestimated at $a_1 = 0$ by about 1.5%. Even though the curves in Fig. 8(b) do reach zero at $a_1 = 1$, it appears that there is no universal power law analogous to that of circle maps [13] for these forced maps. The incommensurate fraction drops to a small value at the onset of weak chaos, and this onset point decreases as a_2 grows. Moreover the shape of these curves below this onset varies as a_2 increases. The proportion of weakly chaotic orbits (black curves) grows substantially with a_2 , reaching 60% when $(a_1, a_2) \approx (1.75, 5)$. This is at the expense of the resonant

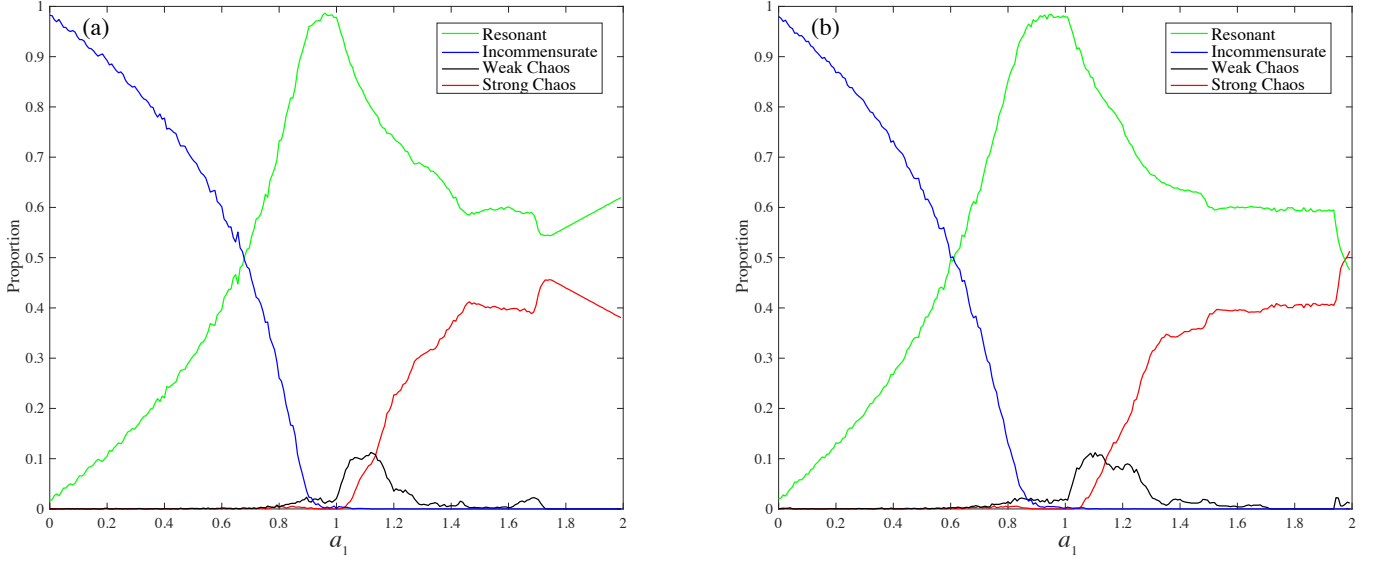


Figure 7: The proportion of strongly chaotic (red), weakly chaotic (black), resonant (green), and incommensurate (blue) orbits for (1) with (2) as a function of a_1 . (a) $a_2 = 0.6$ and (b) $a_2 = 1$.

orbits: each of the green curves peaks near $a_1 = 1$ and decreases thereafter. The resonant proportion falls to near zero at $(a_1, a_2) \approx (2, 5)$ as the chaotic fraction grows.

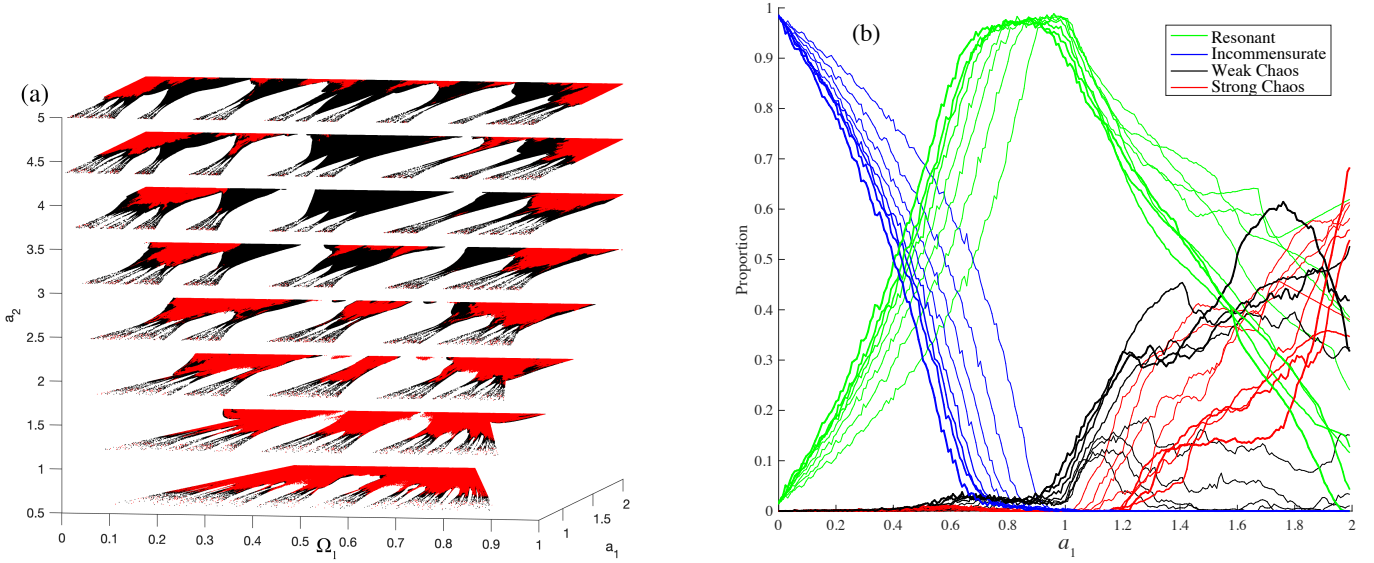


Figure 8: Types of orbits for a grid of eight $a_2 \in [0.6, 5]$ as a function of (a_1, Ω_1) for (1) with (2). (a) Parameter regions with strongly (red) and weakly (black) chaotic orbits. The range $a_1 \in (0.6, 1)$ is shown since the chaotic fractions are negligible for smaller a_1 values. (b) Proportion of the four orbit types as a function of a_1 for each of the eight a_2 values of panel (a) using the color scheme of Fig. 7. The thickness of the eight curves increases with a_2 .

6. Conclusions

In this paper, we used efficient, high-precision numerical techniques to characterize the dynamics of a quasiperiodically-forced extension of the Arnold circle map. An advantage of the weighted Birkhoff average (WBA) (A.2) is that it can rapidly compute the rotation vector, as well as the time average of other phase space functions [37, 32], to near machine precision when the orbit is regular: it is super-convergent when the orbit is smoothly conjugate to a rigid Diophantine rotation [10]. We observed that the computations are even more rapidly convergent when the rotation vector is resonant, recall Fig. 6(b).

We used the WBA to distinguish between chaotic and regular orbits by defining a threshold for the precision, dig_T (A.4), after a fixed number of iterates T . Given an accurate value for rotation vector ω_T (6), we determined if the vector is nearly resonant by finding the smallest order of an integer resonance plane within a distance δ . This allows us to characterize regular orbits as incommensurate (nonresonant) or rank-one (resonant). We used a similar, but more efficient method—based on the Farey tree—for a scalar frequency in [37]. We hope that an efficient algorithm to compute (B.4) for higher dimensional cases can be found. Meanwhile, we used a brute force method, following our previous work on volume-preserving maps [32]. The (m, n) resonances correspond to tongues or mode-locking regions, recall Fig. 3, and we observed that the pinching of these as a function of the coupling parameter, previously reported for low-order resonances, also occurs at higher orders as well as for nonzero m_2 .

Our method gives a new characterization of strange nonchaotic attractors (SNA) and an efficient way to distinguish these from chaos, recall Figs. 4-5. We identify SNAs as invariant sets that are “weakly chaotic”: orbits for which the WBA converges slowly but the Lyapunov exponent is not positive. We showed that the WBA can also be used to improve the accuracy of Lyapunov exponents over the simplest method (9)—though this does not give the super-convergence seen for Diophantine rotations. We hope to investigate the computation of Lyapunov exponents in more detail in a future paper.

Using the method above, we were able to efficiently classify the trajectories of quasiperiodically forced circle maps into four categories: resonant, incommensurate, weakly chaotic, and strongly chaotic, and—as in Figs. 7-8—showed how their proportions vary with the strength of the nonlinearity.

We plan to report on the application of these methods to fully coupled torus maps in another paper [38].

Appendices

Appendix A. Weighted Birkhoff Averages

We briefly review here the weighted Birkhoff average [7, 8, 9] and how to use it to distinguish between regular and chaotic orbits [37]. Given a map $f : M \rightarrow M$, recall that the time average of a function $h : M \rightarrow \mathbb{R}$ along an orbit of f is simply

$$B(h)(z) = \lim_{T \rightarrow \infty} \frac{1}{T} \sum_{t=0}^{T-1} h \circ f^t(z), \quad (\text{A.1})$$

if this limit exists. Under the assumptions that μ is an f -invariant probability measure ($\mu(A) = \mu(f^{-1}(A))$ for any Borel subset A of M), μ is ergodic, and $h \in L^1(M, \mathbb{R})$, then Birkhoff's ergodic theorem implies that

$$B(h)(z) = \langle h \rangle = \int_M h d\mu$$

for μ -almost every z . However, the convergence to this limit is at best as $1/T$ [23] and can be arbitrarily slow [25].

To compute the average efficiently and accurately for a length- T segment of an orbit, we modify (A.1) using the C^∞ weight function³

$$\Psi(s) \equiv \begin{cases} e^{-[s(1-s)]^{-1}} & s \in (0, 1) \\ 0 & s \leq 0 \text{ or } s \geq 1 \end{cases}.$$

This exponential bump function converges to zero with infinite smoothness at 0 and 1, i.e., $\Psi^{(k)}(0) = \Psi^{(k)}(1) = 0$ for all $k \in \mathbb{N}$. The finite-time weighted Birkhoff average (WBA) is then defined by

$$WB_T(h)(z) = \frac{1}{S} \sum_{t=0}^{T-1} \Psi\left(\frac{t}{T}\right) h \circ f^t(z), \quad (\text{A.2})$$

with the normalization constant

$$S \equiv \sum_{t=0}^{T-1} \Psi\left(\frac{t}{T}\right). \quad (\text{A.3})$$

As shown in [7], (A.2) gives the same answer as $T \rightarrow \infty$ as (A.1); however, for regular orbits it can converge much more quickly. In particular, if the orbit is conjugate to a rigid rotation with a Diophantine rotation vector ω and the map f and function h are C^∞ , then (A.2) converges faster than any power [8]:

$$|WB_T(h) - \langle h \rangle| < \frac{c_k}{T^k}, \quad \forall k \in \mathbb{N}.$$

We estimate the error of the WBA for a given function h and a given time T by computing the effective number of digits of accuracy:

$$\text{dig}_T = -\log_{10} |WB_T(h)(z) - WB_T(h)(f^T(z))|, \quad (\text{A.4})$$

i.e., comparing the result for the first T iterates with that for the next T iterates. In [37], we observed that for the 2D Chirikov standard map, dig_T converges rapidly to machine precision for orbits that lie on invariant

³Optimal choices for the weighting function have recently been explored by Ruth and Bindel using reduced rank extrapolation [35].

circles: double precision accuracy ($\text{dig}_T \sim 14$) for most orbits is obtained within $T \approx 10^4$ iterates. However, it converges slowly, or not at all for chaotic orbits. When the map has mixtures of regular and chaotic orbits, a histogram of dig_{10^4} , [37, Fig. 3] shows two peaks, a broader one around $\text{dig}_T = 2$, corresponding to chaotic orbits and a narrower one around $\text{dig}_T = 14$, that corresponds to regular orbits. The latter peak has a tail over the interval $6 < \text{dig}_T < 13$: for these orbits the average converges more slowly. Such orbits typically lie near the boundary of narrow chaotic layers or are periodic with high period within lower-period island chains. In [37] we showed our method is as accurate and more efficient than two standard methods for identifying chaos: a positive Lyapunov exponent and the 0-1 test for chaos. In [32] we used the WBA to study two-tori in a 3D volume-preserving map.

To obtain a criterion distinguishing chaotic and regular orbits, we choose a cutoff value for dig_T , declaring that

$$\text{dig}_T < D_T \Rightarrow \text{“chaotic”} ; \quad (\text{A.5})$$

conversely, all orbits with $\text{dig}_T > D_T$ are “nonchaotic”. In [32] we chose the cutoff $D_{10^6} = 11$ for a 3D map where the tori can be 1D or 2D. This cutoff is conservative in the sense that a chaotic orbit will be not be identified as regular, but there is a possibility of a regular orbit will be misidentified as chaotic. This choice had the benefit that the rotation vector of any orbit identified as regular can be computed with high accuracy, and in that paper we were interested in studying the number theoretic properties of the robust tori. For the current paper we use the less strict criterion

$$T = 10^6, \quad D_T = 9, \quad (\text{A.6})$$

which is still conservative in that chaotic orbits are quite unlikely to be identified as regular.

Appendix B. Resonance Orders

In addition to providing the distinction between regular and chaotic orbits, the WBA can be used to compute an accurate value of the time average of a function h of interest. In particular, we can compute the rotation vector (3) of an orbit for a torus map of the form (1) using (6). If T is large enough and the rotation vector exists, we expect $\omega_T \approx \omega(x, f)$. Of course, for the quasiperiodic case, (4) implies that we only need to compute the first component of (6).

In general the resulting frequency vector can be rational, commensurate, or incommensurate. To estimate whether a computed vector is essentially rational we would ask that $\left| \omega - \frac{p}{q} \right|$ be small for $p \in \mathbb{Z}^d$, $q \in \mathbb{N}$; this would correspond to finding a rational approximation of the vector ω . More generally, $\omega \in \mathbb{R}^d$ has a *commensurability* (or is *resonant* or *mode-locked*) if there is an $m \in \mathbb{Z}^d \setminus \{0\}$ and an $n \in \mathbb{Z}$ such that

$$\omega \in \mathcal{R}_{m,n} = \{ \alpha \in \mathbb{R}^d : m \cdot \alpha = n \}, \quad (\text{B.1})$$

i.e., it lies in the codimension-one plane $\mathcal{R}_{m,n}$. We say that ω has *resonance order* M if it satisfies (B.1) and $M = \|m\|_1$ is the smallest length of such a (nonzero) vector m . The set of vectors that do not lie in any plane are *incommensurate*; an example is $\omega = (\sqrt{2}, \sqrt{5})$.

For $d = 2$, the sets $\mathcal{R}_{m,n}$ are lines. The *rank* of the resonance for a given ω is the number of independent commensurability vectors m ; i.e., the dimension of the module of resonance vectors. Note that ω is rational only if the rank is d ; commensurabilities that have lower rank are partially resonant, such as the rank-one vector $\omega = (3\sqrt{2}, 2\sqrt{2} - 1)$ which lies in $\mathcal{R}_{(2,-3),3}$ so that $M = 5$.

A vector ω is then *approximately* commensurate if $|m \cdot \omega - n|$ is small, and in [32] we developed a method for computing such commensurabilities. We say that a vector ω is (m, n) -resonant *to precision* δ if the resonant plane intersects a ball of radius δ about ω :

$$\mathcal{R}_{m,n} \cap B_\delta(\omega) \neq \emptyset. \quad (\text{B.2})$$

Using the Euclidean norm, the minimum distance between the plane (B.1) and the point ω is

$$\Delta_{m,n}(\omega) = \min_{\alpha \in \mathcal{R}_{m,n}} \|\alpha - \omega\|_2 = \frac{|m \cdot \omega - n|}{\|m\|_2}. \quad (\text{B.3})$$

Thus ω is (m, n) resonant to precision δ , whenever $\Delta_{m,n}(\omega) < \delta$, and we call the value

$$M(\omega, \delta) = \min\{\|m\|_1 : \Delta_{m,n}(\omega) < \delta, m \in \mathbb{Z}^d \setminus \{0\}, n \in \mathbb{Z}\}, \quad (\text{B.4})$$

the *resonance order* of ω .

As far as we know, there is no generalization of the $d = 1$ Farey tree result used in [37] to compute (B.4) efficiently.⁴ Nevertheless, since there are finitely many $m \in \mathbb{Z}^d$ such that $\|m\|_1 \leq M$, a brute force computation is of course possible for modest values of M ; we gave such an algorithm in [32].

To understand what resonance orders are “typical,” in [32] we computed the minimal resonance order (B.4) for a set of equi-distributed, random $\omega \in [0, 1]^2$ as a function of the precision δ . The resulting distribution of $\log(M)$ seen in [32, Fig. 8] has a mean and standard deviation

$$\begin{aligned} \langle \log_{10} M(\omega, \delta) \rangle &= -0.334 \log_{10}(\delta) - 0.091, \\ \sigma &= 0.171. \end{aligned} \quad (\text{B.5})$$

We observed that the standard deviation seems to be essentially independent of δ , and we found a similar result for $d = 1$ in [37]. Our computations inspired Chen and Haynes [5] and more recently Marklof [30, 31] to find rigorous results for the resonance order distributions.

Since the cutoff (A.6) gives rotation number calculations accurate to within 10^{-9} , we choose $\delta = 10^{-9}$ for (B.4). For this case, (B.5) implies that $\langle \log_{10} M \rangle = 2.915$. We declare that a vector is nonresonant if

$$256 \leq M \leq 2673 \Rightarrow \text{“nonresonant”}, \quad (\text{B.6})$$

corresponding to $2.407 < \log_{10}(M) < 3.427$, which is a range of approximately $\pm 3\sigma$ about the mean (B.5). To test this criterion we selected 10^4 uniformly randomly distributed values in $[0, 1]^2$, and found that 1.36% were incorrectly identified as resonant. Note that the distribution of log-orders for random vectors is not symmetric around the mean; in particular, $M < 256$ occurred 1.32% of the time, and $M > 2673$ occurred 0.04% of the time.

We can further categorize the *resonant* orbits (those that fail Criterion (B.6)) by the rank of the resonance. Rank-two resonant orbits have frequencies on the intersection of a pair of different resonance lines. For the quasiperiodic case we study here, $\omega_2 = \Omega_2$ is irrational; therefore, all resonant orbits will have rank one.

References

- [1] Alsedà, L., Borros-Cullell, S., 2021. An algorithm to compute rotation intervals of circle maps. Commun. Nonl. Sci. Numer. Sim. 102, 105915. <https://doi.org/10.1016/j.cnsns.2021.105915>.
- [2] Ashwin, P., Guaschi, J., Phelps, J., 1993. Rotation sets and phase-locking in an electronic three oscillator system. Physica D 66, 392–411. [https://doi.org/10.1016/0167-2789\(93\)90075-C](https://doi.org/10.1016/0167-2789(93)90075-C).
- [3] Bjerklöv, K., Jäger, T., 2009. Rotation numbers for quasiperiodically forced circle maps—mode-locking vs string monotonicity. J. American Math. Soc. 22, 353–362. <https://www.jstor.org/stable/40587236>.

⁴The Kim-Ostlund tree can be used to get resonance relations [2]; however, it is not clear that this algorithm returns a minimal $\|m\|$.

- [4] Blessing, D., James, J.D.M., 2023. Weighted Birkhoff averages and the parameterization method. [arXiv:2306.16597](https://arxiv.org/abs/2306.16597). <https://arxiv.org/abs/2306.16597>.
- [5] Chen, H., Haynes, A., 2023. Expected value of the smallest denominator in a random interval of fixed radius. *Int. J. Number Theory* <https://doi.org/10.1142/S1793042123500689>.
- [6] Das, S., Dock, C., Saiki, Y., Salgado-Flores, M., Sander, E., Wu, J., Yorke, J., 2016a. Measuring quasiperiodicity. *Euro. Phys. Lett.* 114, 40005. <https://doi.org/10.1209/0295-5075/114/40005>.
- [7] Das, S., Saiki, Y., Sander, E., Yorke, J., 2016b. Quasiperiodicity: Rotation numbers, in: Skiadas, C. (Ed.), *Foundations of Chaos Revisited: From Poincaré to Recent Advancement*. Springer. Understanding Complex Systems, pp. 103–118. https://doi.org/10.1007/978-3-319-29701-9_7.
- [8] Das, S., Saiki, Y., Sander, E., Yorke, J., 2017. Quantitative quasiperiodicity. *Nonlinearity* 30, 4111. <https://doi.org/10.1088/1361-6544/aa84c2>.
- [9] Das, S., Saiki, Y., Sander, E., Yorke, J., 2019. Solving the Babylonian problem of quasiperiodic rotation rates. *Disc. Cont. Dyn. Sys.* 12, 2279–2305. <https://doi.org/10.3934/dcdss.2019145>.
- [10] Das, S., Yorke, J., 2018. Super convergence of ergodic averages for quasiperiodic orbits. *Nonlinearity* 31, 491–501. <https://doi.org/10.1088/1361-6544/aa99a0>.
- [11] Ding, M., Grebogi, C., Ott, E., 1989. Evolution of attractors in quasiperiodically forced systems: From quasiperiodic to strange nonchaotic to chaotic. *Phys. Rev.* 39A, 2593–2598. <https://doi.org/10.1103/physreva.39.2593>.
- [12] Duignan, N., Meiss, J.D., 2023. Distinguishing between regular and chaotic orbits of flows by the weighted Birkhoff average. *Physica D* 449, 133749. <https://doi.org/10.1016/j.physd.2023.133749>.
- [13] Ecke, R., Farmer, J., Umberger, D., 1989. Scaling of the Arnold tongues. *Nonlinearity* 2, 175–196. <https://doi.org/10.1088/0951-7715/2/2/001>.
- [14] Feudel, U., Grebogi, C., Ott, E., 1997. Phase-locking in quasiperiodically forced systems. *Physics Reports* 290, 11–25. [https://doi.org/10.1016/S0370-1573\(97\)00055-0](https://doi.org/10.1016/S0370-1573(97)00055-0).
- [15] Feudel, U., Kurths, I., Pikovsky, A., 1995. Strange non-chaotic attractor in a quasiperiodically forced circle map. *Physica D* 88, 176–186. [https://doi.org/10.1016/0167-2789\(95\)00205-1](https://doi.org/10.1016/0167-2789(95)00205-1).
- [16] Glendinning, P., Feudel, U., Pikovsky, A.S., Stark, J., 2000. The structure of mode-locked regions in quasi-periodically forced circle maps. *Physica D* 140, 227–243. [https://doi.org/10.1016/S0167-2789\(99\)00235-3](https://doi.org/10.1016/S0167-2789(99)00235-3).
- [17] Glendinning, P., Jäger, T., Keller, G., 2006. How chaotic are strange non-chaotic attractors? *Nonlinearity* 19, 2005–2022. <https://doi.org/10.1088/0951-7715/19/9/001>.
- [18] Glendinning, P., Jäger, T., Stark, J., 2009. Strangely dispersed minimal sets in the quasiperiodically forced Arnold circle map. *Nonlinearity* 22, 835–854. <https://doi.org/10.1088/0951-7715/22/4/008>.
- [19] Grebogi, C., Ott, E., Pelikan, S., Yorke, J., 1984. Strange attractors that are not chaotic. *Physica D* 13, 261–268. [https://doi.org/10.1016/0167-2789\(84\)90282-3](https://doi.org/10.1016/0167-2789(84)90282-3).
- [20] Haro, A., Canadell, M., Figueras, J.L., Josep, A.L., Mondelo, M., 2016. *The Parameterization Method for Invariant Manifolds from Rigorous Results to Effective Computations*. Springer International. <https://doi.org/10.1007/978-3-319-29662-3>.

- [21] Herman, M., 1983. Une méthode pour minorer les exposants de Lyapunov et quelques exemples montrant le caractère local d'un théorème d'Arnold et de Moser sur le tore de dimension 2. *Comment. Math. Helv.* 58, 453–502. <https://doi.org/10.1007/BF02564647>.
- [22] Jäger, T., Stark, J., 2006. Towards a classification for quasiperiodically forced circle homeomorphisms. *J. London. Math. Soc.* 73, 727–744. <https://doi.org/10.1112/S0024610706022782>.
- [23] Kachurovskii, A., 1996. The rate of convergence in ergodic theorems. *Russian Mathematical Surveys* 51, 653. <https://doi.org/10.1070/RM1996v051n04ABEH002964>.
- [24] Kim, J., Kim, S., Hunt, B., Ott, E., 2003. Fractal properties of robust strange nonchaotic attractors in maps of two or more dimensions. *Phys. Rev. E* 67, 036211. <https://doi.org/10.1103/PhysRevE.67.036211>.
- [25] Krengel, U., 1978. On the speed of convergence in the ergodic theorem. *Monatshefte für Mathematik* 86, 3–6. <https://doi.org/10.1007/BF01300052>.
- [26] Laskar, J., 1993. Frequency analysis for multi-dimensional systems. *global dynamics and diffusion. Physica D* 67, 257–283. [https://doi.org/10.1016/0167-2789\(93\)90210-R](https://doi.org/10.1016/0167-2789(93)90210-R).
- [27] Laskar, J., 2003. Frequency map analysis and particle accelerators, in: *Proceedings of the 2003 Ieee Particle Accelerator Conference (Pac 03)*. IEEE, pp. 378–382. <http://adsabs.harvard.edu/abs/2003pac.conf..378L>.
- [28] Luque, A., Villanueva, J., 2008. Computation of derivatives of the rotation number for parametric families of circle diffeomorphisms. *Physica D* 237, 25992615. <https://doi.org/10.1016/j.physd.2008.03.047>.
- [29] Luque, A., Villanueva, J., 2014. Quasi-periodic frequency analysis using averaging-extrapolation methods. *SIAM J. Dyn. Syst.* 13, 1–46. <https://doi.org/10.1137/130920113>.
- [30] Marklof, J., 2024a. The log moments of smallest denominators. *Zenodo* 24, 1–13. <https://doi.org/10.5281/zenodo.12167470>.
- [31] Marklof, J., 2024b. Smallest denominators. *Bull. London Math. Soc.* 56, 1920–1938. <https://londmathsoc.onlinelibrary.wiley.com/doi/10.1112/blms.13034>.
- [32] Meiss, J.D., Sander, E., 2021. Birkhoff averages and the breakdown of invariant tori in volume-preserving maps. *Physica D* 428, 133048. <https://doi.org/10.1016/j.physd.2021.133048>.
- [33] Osinga, H., Wiersig, J., Glendinning, P., Feudel, U., 2001. Multistability in the quasiperiodically forced circle map. *Int. J. Bif. Chaos* 11, 3085–3105. <https://doi.org/10.1142/S0218127401004029>.
- [34] Polotzek, K., Padberg-Gehle, K., Jäger, T., 2017. Set-oriented numerical computation of rotation sets. *J. Comp. Dyn.* 4, 119–141. <https://doi.org/10.3934/jcd.2017004>.
- [35] Ruth, M., Bindel, D., 2024. Finding Birkhoff Averages Via Adaptive Filtering. Technical Report. Cornell University. <https://arxiv.org/abs/2403.19003>.
- [36] Sanchez, J., Net, M., Simo, C., 2010. Computation of invariant tori by Newton–Krylov methods in large-scale dissipative systems. *Physica D* 239, 123–133. <https://doi.org/10.1016/j.physd.2009.10.012>.
- [37] Sander, E., Meiss, J., 2020. Birkhoff averages and rotational invariant circles for area-preserving maps. *Physica D* 411, 132569. <https://doi.org/10.1016/j.physd.2020.132569>.

- [38] Sander, E., Meiss, J., 2024. Nonuniversality of the fraction of regular orbits for torus maps. in preparation .
- [39] Sander, E., Yorke, J., 2015. The many facets of chaos. *Internat. J. Bifur. Chaos* 25, 1530011, 15. doi:[10.1142/S0218127415300116](https://doi.org/10.1142/S0218127415300116). <https://doi.org/10.1142/S0218127415300116>.
- [40] Seara, T., Villanueva, J., 2006. On the numerical computation of Diophantine rotation numbers of analytic circle maps. *Physica D* 217, 107–120. <https://doi.org/10.1016/J.Physd.2006.03.013>.
- [41] Seara, T., Villanueva, J., 2009. Numerical computation of the asymptotic size of the rotation domain for the Arnold family. *Physica D* 238, 197–208. <https://doi.org/10.1016/J.Physd.2008.09.002>.
- [42] Stark, J., Feudel, U., Glendinning, P., Pikovsky, A., 2002. Rotation numbers for quasiperiodically forced monotone circle maps. *Dyn. Syst.* 17, 1–28. <http://doi.org/10.1080/14689360110073641>.
- [43] Sturman, R., 1999. Scaling of intermittent behaviour of a strange nonchaotic attractor. *Physics Letters A* 259, 355–365. [https://doi.org/10.1016/S0375-9601\(99\)00463-6](https://doi.org/10.1016/S0375-9601(99)00463-6).
- [44] Villanueva, J., 2022. A new averaging-extrapolation method for quasi-periodic frequency refinement. *Physica D* 438, 133344. <https://doi.org/10.1016/j.physd.2022.133344>.